This is the accepted manuscript made available via CHORUS. The article has been published as:

Novel family of topological semimetals with butterflylike nodal lines

Xiaoting Zhou, Chuang-Han Hsu, Hugo Aramberri, Mikel Iraola, Cheng-Yi Huang, Juan L. Mañes, Maia G. Vergniory, Hsin Lin, and Nicholas Kioussis

Phys. Rev. B **104**, 125135 — Published 22 September 2021

DOI: 10.1103/PhysRevB.104.125135

Novel Family of Topological Semimetals with Butterfly-like Nodal Lines

Xiaoting Zhou,[1,*] Chuang-Han Hsu,[2] Hugo Aramberri,[1] Mikel Iraola,[3,4] Cheng-Yi Huang,[5,1] Juan L. Mañes,[4] Maia G. Vergniory,[3,6] Hsin Lin,[5] and Nicholas Kioussis[1,†]

[1]*Department of Physics and Astronomy, California State University, Northridge, CA 91330, USA*
[2]*Department of Electrical and Computer Engineering, Faculty of Engineering, National University of Singapore, Singapore 117583*
[3]*Donostia International Physics Center, 20018 Donostia-San Sebastian, Spain*
[4]*Department of Condensed Matter Physics, University of the Basque Country UPV/EHU, Apartado 644, 48080 Bilbao, Spain*
[5]*Institute of Physics, Academia Sinica, Taipei 11529, Taiwan*
[6]*IKERBASQUE, Basque Foundation for Science, Maria Diaz de Haro 3, 48013 Bilbao, Spain*

(Dated: September 13, 2021)

In recent years, the exotic properties of topological semimetals (TSMs) have attracted great attention and significant efforts have been made in seeking for new topological phases and material realization. In this work, we propose a new family of TSMs which harbors an unprecedented nodal line (NL) landscape consisting of a pair of concentric intersecting coplanar ellipses (CICE) at half-filling. Meanwhile, the CICE at half-filling guarantees the presence of a second pair of CICE beyond half-filling. Both CICEs are linked at four-fold degenerate points (FDPs) at zone boundaries. In addition, we identify the generic criteria for the existence of the CICE in a time reversal invariant *spinless* fermion system or a spinfull system with negligible spin-orbital coupling (SOC). Consequently, 9 out of 230 space groups (SGs) are feasible for hosting CICE whose location centers in the first Brillouin zone (BZ) are identified. We provide a simplest model with SG *Pbam* (No. 55) which exhibits CICE, and the exotic intertwined drumhead surface states, induced by double-band-inversions. Finally, we propose a series of material candidates that host butterfly-like CICE NLs, such as, ZrX_2 (X=P,As), Tl_2GeTe_5, CYB_2 and Al_2Y_3.

INTRODUCTION

Topological semimetals (TSMs) [1–4]have emerged among the most active frontiers in condensed matter physics in recent years, drawing widespread attention from both the theoretical and the experimental communities. In the noninteracting limit, TSMs describe systems which are characterized by the topologically robust band-crossings manifolds between conduction and valence bands in momentum k space. These mainfolds can be zero-dimensional (0D) nodal points, *e.g.,* three-dimensional (3D) Weyl semimetals (WSMs) [4–6] and Dirac semimetals (DSMs) [4, 7–11], and one-dimensional (1D) nodal lines/loops, *e.g.,* nodal-line semimetals (NLSMs) [2, 12]. Around these band-crossings, electron excitations behave drastically differently from the conventional Schrödinger fermions in normal metals. For example, the low-energy electrons in 3D DSMs and WSMs resemble the relativistic Dirac and Weyl fermions, making it possible to mimic high-energy physics phenomena. Meanwhile, TSMs are distinguished from normal semimetals by the accompanying topological indices due to the aforementioned manifolds. Moreover, because of these unique electronic features, TSMs present exotic properties in different ways, such as Fermi arcs [13] and drumhead surface states (SSs) [14] on surfaces of WSMs and NLSMs, respectively, and novel transport phenomena *e.g.,* the negative magnetoresistance related to the chiral anomaly in both Weyl and Dirac SMs [15–17].

Among TSMs, NLSMs possess the highest variability. Nodal lines (NLs) can be integrated in various configurations, *e.g.,* a chain link [11, 18–20], a Hopf link [19], and a knot [21], where each of them carries its unique topology. Since the essential characteristics, band crossings, of various TSMs are mostly protected by crystalline symmetries, a thorough classification of a particular type of TSMs in all space groups can greatly accelerate the experimental discovery. There exist well-established classifications for DSMs and WSMs [22–24], and the triple point semimetals [25]. However, for most types of NLSMs proposed today, except the chain link [18] and some types of intersecting rings [26], the symmetry criteria of the emergence of particular nodal lines remain deficient.

In this Letter, we introduce a new type of NLSM in time-reversal invariant *spinless* systems, which hosts a butterfly-like nodal-line (NL) consisting of a pair of concentric intersecting coplanar ellipses (CICE) at half-filling residing on a plane in k space, as indicated by the blue, red concentric ellipses in Fig.1(a). Meanwhile, the half-filling CICE consequently guarantees the presence of another pair of CICE formed by band crossings beyond half-filling, which is indicated by the magenta lines in Fig.1(b). We demonstrate that CICE can be sustained by nonsymmorphic crystalline symmetries including two glide symmetries, and only 9 space groups (SGs) are feasible to host it. These SGs are classified into two categories by their point group symmetries, which are D_{2h} and D_{4h}. Moreover, we provide a tight-binding model for one of the SGs *Pbam* (No. 55) which exhibits CICE and hosts exotic intertwined drumhead surface states. In the end, five material candidates from these two categories, host-

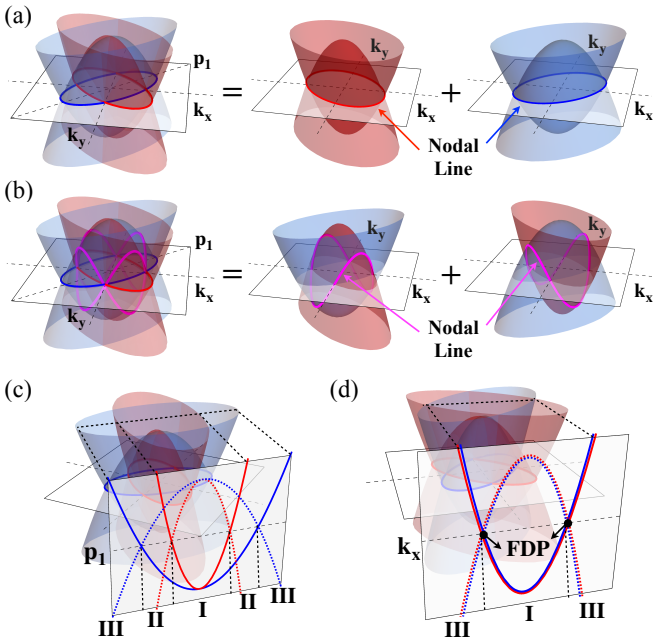

FIG. 1. Schematic band structures showing the mechanism of the formation of the CICE NLs, resulting from the DBI. (a) The half-filling CICE can be decomposed into two ellipses in red and blue, respectively, which are locked by symmetries. Each ellipse is the band-crossing due to a single band inversion and protected by mirror (or glide) symmetry $\mathcal{M}_z$ (or $\mathcal{G}_z$). (b) The second pair of CICE NLs (labeled in magenta) emerge due to the crossings between the bands denoted in red and blue corresponding to crossings between two occupied (one-quarter filling) or two unoccupied (three-quarter filling) bands. These cross the Fermi surface (FS) leading to the intersection of four NLs at four points on the k_x and k_y axes. Band structures along the paths (c) p_1 and (d) k_x-axis. The bands labeled by solid and dashed lines carry different eigenvalues of $\mathcal{M}_z$ (or $\mathcal{G}_z$), and opposite parity at the center TRIM point of the CICE. Bands are doubly degenerate along k_x-axis (d) and similarly, along k_y-axis. I, II and III denote the regions divided by the NLs.

ing the proposed CICE, are suggested for further experimental studies, such as time-resolved angle-resolved photoemission spectroscopy and studies of magneto-optical effects. [27, 28]

SYMMETRY CRITERIA AND SPACE GROUPS

Conceptually, a pair of CICE can be constructed by integrating two NL fermions. As shown in Fig. 1(a), CICE denoted by the intersection of the red and blue ellipses on the $k_z = 0$ plane can be decomposed into two individual NL fermions. Each NL, the accidental two-fold band-crossings due to the band inversion, is further validated by the inherent crystal symmetry belonging to its parent bands, which is the mirror (or glide) reflection symmetry, $\mathcal{M}_z(\mathcal{G}_z) : (k_x, k_y, k_z) \to (k_x, k_y, -k_z)$. On the $k_z = 0$ plane, states (labeled by solid and dashed lines in Fig. 1(c)) carrying different mirror (or glide) eigenvalues forbid their mutual hybridization, thus supporting the NL fermion. Since at each k point $\mathcal{M}_z$ ($\mathcal{G}_z$) only supplies two different eigenvalues, additional symmetry constrains along k_x and k_y axes are demanded to sustain the four-fold degenerate points (FDPs) on the CICE, *i.e.*, the intersecting points of the two NL fermions, marked in Fig. 1(d).

TABLE I. List of space groups (SGs) and corresponding point groups (PGs) that can host CICE. We also list the possible positions of the CICE centers and the axes on which the four-fold degenerate points on the CICE emerge.

PGs	SGs (#)	Positions	Axes
D_{2h}	*Pbam* (55)	$(\pi,\pi,0)$, (π,π,π)	{[100], [010]}
	Pccn (56)	(π,π,π)	
	Pnnm (58)	$(\pi,\pi,0)$	
	Pnma (62)	$(\pi,0,\pi)$	{[100], [001]}
D_{4h}	$P4/mbm$ (127)	$(\pi,\pi,0)$, (π,π,π)	{[100], [010]}
	$P4/mnc$ (128)	$(\pi,\pi,0)$	
	$P4_2/mbc$ (135)	$(\pi,\pi,0)$	
	$P4_2/mnm$ (136)	$(\pi,\pi,0)$	
	$P4_2/ncm$ (138)	(π,π,π)	

Therefore, the additional symmetries required along k_x and k_y to guarantee the two-fold degeneracy can be realized by introducing an antiunitary symmetry, $\mathcal{TQ}$, which combines time-reversal symmetry (TRS) $\mathcal{T}$ and a spatial symmetry $\mathcal{Q}$. Thus, the Kramer-like two-fold degeneracy is enforced at $\mathcal{TQ}$-invariant points where $(\mathcal{TQ})^2 = -1$. For a *spinless* system, $\mathcal{T}^2 = +1$, which in turn requires that $\mathcal{Q}$ is a nonsymmorphic symmetry, with eigenvalues of $\pm i$ [9, 29] at certain points on the boundaries of BZ. Consequently, the qualified candidates of $\mathcal{Q}$ for ensuring the degeneracy on the k_x (k_y) are, $\mathcal{G}_x$ or $\mathcal{S}_y$ ($\mathcal{G}_y$ or $\mathcal{S}_x$), so the CICE should be centered at $(\pi, \pi, 0$ or $\pi)$. Here, $\mathcal{S}_{x(y)} = \{\mathcal{C}_{2x(2y)}|\boldsymbol{t}_{x(y)}\}$ denotes a two-fold screw rotation with respect to the $k_{x(y)}$-axis accompanied by a translation $\boldsymbol{t}_{x(y)} = \frac{1}{2}\hat{x}(\hat{y})$, and $\mathcal{G}_{x(y)} = \{\mathcal{M}_{x(y)}|\boldsymbol{t}_{y(x)}\}$ is a glide symmetry normal to $k_{x(y)}$, which contains a fractional translation $\boldsymbol{t}_{y(x)} = \frac{1}{2}\hat{y}(\hat{x})$. To avoid replicas of CICE on other symmetry-related planes, n-fold rotation and rotoinversion symmetries with $n > 2$ with respect to the $k_{x(y)}$ axes are not allowed. In addition, each Kramer-paired states should carry the same mirror symmetry eigenvalue of $\mathcal{M}_z$ (or $\mathcal{G}_z$). Furthermore, symmetry-enforced degeneracy are not allowed at any generic point of the $k_z = 0$ plane other than the $k_{x(y)}$-axis.

In summary, the criteria for generating CICE in a *spinless* crystal preserving TRS include: (i) the little group of the center of CICE is nonsymmorphic with corresponding point group (PG) D_{2h} or D_{4h}; (ii) the crystal contains two glide $\mathcal{G}_{x(y)}$ or screw $\mathcal{S}_{y(x)}$ symmetries with respect to the axes lying on a mirror $\mathcal{M}_z$ or a glide $\mathcal{G}_z$ plane; (iii) at the center of the CICE, $\mathcal{M}_z$ ($\mathcal{G}_z$) should commute with other preserved and required symmetries. According to the above criteria, we have exhaustively scanned all 230 SGs, and determined 9 possible SGs to host CICE. The corresponding positions of the center of the CICE and the corresponding axes of $\mathcal{S}$ or $\mathcal{G}$ are listed in Table. I.

LATTICE MODEL AND SURFACE STATES

To validate the criteria derived above and explore the underlying topology of CICE, we construct a minimal 4-band tight-binding lattice model for the SG *Pbam* (No. 55). The minimal required symmetries are $\mathcal{M}_z = \{m_{001}|000\}$, $\mathcal{G}_x = \{m_{100}|\frac{1}{2}\frac{1}{2}0\}$ and $\mathcal{G}_y = \{m_{010}|\frac{1}{2}\frac{1}{2}0\}$. The model is a bipartite lattice, where the sublattices denoted by A (gray) and B (blue) occupy the 2a Wyckoff position at $\mathbf{r}_A = (0,0,0)$ and $\mathbf{r}_B = (\frac{1}{2},\frac{1}{2},0)$ in a unit cell (see Fig. 2 (a) for the structure). Each sublattice contains two orbitals, p_z and d_{xy} described by the Pauli matrix $\boldsymbol{\sigma}$, and $\boldsymbol{\tau}$ for the A and B sublattices (see Appendix A for details). For a *spinless* system, employing the basis $\Psi = (p_z^A, d_{xy}^A, p_z^B, d_{xy}^B)^T$ the symmetry-constrained tight-binding Hamiltonian is of the form,

$$\begin{aligned} H_0(\mathbf{k}) = &[(\alpha \cos k_x + \beta \cos k_y + \gamma \cos k_z) + \delta_0]\tau_0\sigma_3 \\ &+ \cos\frac{k_x}{2}\cos\frac{k_y}{2}\cos k_z(\lambda_{10}\tau_1\sigma_0 + \lambda_{13}\tau_1\sigma_3) \\ &+ \sin k_z(\lambda_{32}\tau_3\sigma_2) \\ &+ \sin\frac{k_x}{2}\sin\frac{k_y}{2}\sin k_z(\lambda_{12}\tau_1\sigma_2), \end{aligned} \tag{1}$$

where $\alpha, \beta, \gamma, \delta_0$, and λ_{ij} are constants.

Since the CICE can emerge on the mirror plane (gray shaded area in Fig. 2(b)) centered at the high symmetry k point $S = (\pi, \pi, 0)$ [$R = (\pi, \pi, \pi)$] (Fig. 2(b)), we derive the effective $k \cdot p$ Hamiltonian around the S(R) point,

$$\begin{aligned} H_{S(R)}(\mathbf{q}) = &\frac{1}{2}(\alpha q_x^2 + \beta q_y^2 \mp \gamma q_z^2 + 2\delta_{S(R)})\tau_0\sigma_3 \\ &+ \frac{1}{4}q_x q_y(\lambda_{10}\tau_1\sigma_0 + \lambda_{13}\tau_1\sigma_3) \\ &+ q_z(\lambda_{12}\tau_1\sigma_2 + \lambda_{32}\tau_3\sigma_2). \end{aligned} \tag{2}$$

At $q_z = 0$, the Hamiltonian is diagonalized as $E_{S(R)}(q_x, q_y, 0) = \mathrm{diag}(E_+^{A+B}, E_-^{A+B}, E_+^{A-B}, E_-^{A-B})$ on the basis $\Psi' = (p_z^{A+B}, d_{xy}^{A+B}, p_z^{A-B}, d_{xy}^{A-B})^T$, where $|\varphi^{A\pm B}\rangle = \frac{1}{\sqrt{2}}(|\varphi^A\rangle \pm |\varphi^B\rangle)$ ($\varphi = p_z, d_{xy}$) denote the bonding/antibonding states of the relevant orbitals. Each ellipse in the half-filling CICE is the line crossing between the conduction band and valence band, which

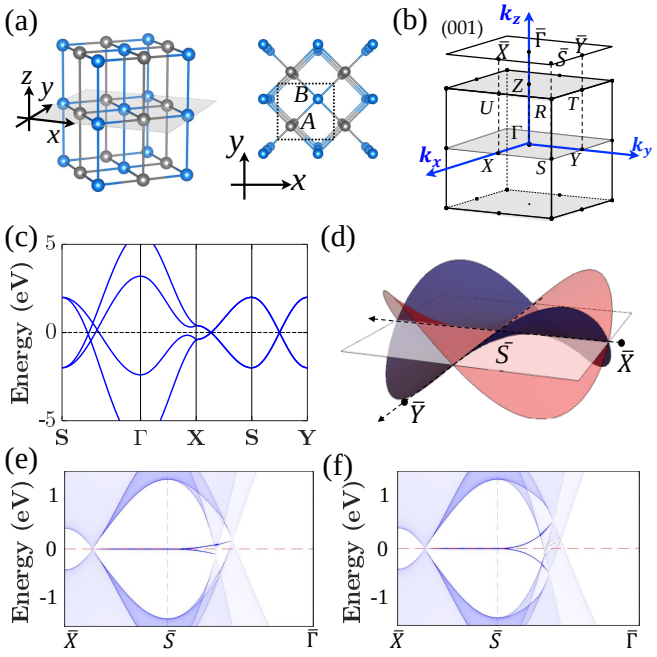

FIG. 2. (a) Orthorhombic crystal structure of the lattice model in Eq.(1) in SG *Pbam*, consisting of a bipartite lattice with two sublattices A (in blue) and B (in gray). (b)Bulk BZ, the projected (001) surface BZ, and high-symmetry points. (c) Band structures of the model without spin-orbit coupling. (d) Schematic dispersion of the drumhead surface states (DSSs) of the (001) surface stemming from the NLs, with two saddle-like hyperbolic paraboloids intertwined with each other. (e-f) Dispersion along high symmetric directions of two types of DSSs on the (001) surface. (e) Type-I DSSs stem from the CICE FS, while (f) type-II from the NLs labeled in magenta in Fig.1(b).

is referred as type-I NL. Whereas, type-II NLs are the crossings between two conduction or two valence bands. If $|\lambda_{13}| > |\lambda_{10}|$, the crossings between the bands E_+^{A+B} (E_+^{A-B}) and E_-^{A+B} (E_-^{A-B}) gives rise to the type-I NL, while E_+^{A+B} (E_+^{A-B}) and E_-^{A-B} (E_-^{A+B}) give rise to the type-II NLs. Otherwise, if $|\lambda_{13}| < |\lambda_{10}|$, type-I NLs evolve to type-II, and vice versa. Thus, the corresponding NLs for the half-filling CICE can be obtained by solving the equations,

$$|\lambda_{13}| > |\lambda_{10}|: \quad \alpha q_x^2 + \beta q_y^2 \pm \frac{1}{2}\lambda_{13} q_x q_y + 2\delta_{S(R)} = 0, \tag{3}$$

$$|\lambda_{13}| < |\lambda_{10}|: \quad \alpha q_x^2 + \beta q_y^2 \pm \frac{1}{2}\lambda_{10} q_x q_y + 2\delta_{S(R)} = 0, \tag{4}$$

After further analyses, we find that when the condition

$$\{\alpha\delta_{S(R)} < 0 \ \cap \ \alpha\beta > 0 \ \cap \ \alpha \neq \beta\} \tag{5}$$

is satisfied, where $\delta_{S,R} = \delta_0 - (\alpha + \beta \mp \gamma)$, the terms in the first line of Eq. (1) describe two concentric elliptic NLs with double band inversions at the S (R) point

(Fig. 1(d)). The terms in the second line in Eq. (1) adjust the anisotropy of each NL, resulting in two twisted elliptic NLs (see dispersion along $k_x = k_y$ in Fig 2(c), where the band width differs in the two original elliptic NLs). The angles of the elliptic NLs with respect to the k_x-axis are determined via $\theta_\pm = \pm\frac{1}{2}\arctan\frac{\lambda}{2(\alpha-\beta)}$, where $\lambda = \max\{|\lambda_{10}|, |\lambda_{13}|\}$.

To explore the unique topological properties of CICE NL, the system is designed to host CICE centered at the S point and to have no additional band inversions at other time-reversal-invariant momentum points (TRIM). Thus, in addition to Eq. 5, the model parameters should be tuned to satisfy the following conditions:

$$\{\delta_S < 0 \cap \delta_R > 0 \cap \delta_\Gamma > max(|\lambda_{10}|, |\lambda_{13}|) \cap \ \delta_Z > max(|\lambda_{10}|, |\lambda_{13}|)\}; \quad (6)$$
$$\text{or}$$
$$\{\delta_S > 0 \cap \delta_R < 0 \cap \delta_\Gamma < min(-|\lambda_{10}|, -|\lambda_{13}|) \cap \ \delta_Z < min(-|\lambda_{10}|, -|\lambda_{13}|)\};$$

where $\delta_{\Gamma,Z} = \delta_0 + (\alpha + \beta \pm \gamma)$. The corresponding band structure is shown in Fig. 2(c), in which the distinctive features of CICE can be recognized by comparing the bands along $S-\Gamma$ and $S-X$ (or $S-Y$). Since CICE are composed by two NLs, and the essential $\mathcal{G}_x$ and $\mathcal{G}_y$ symmetries are preserved on (001) surface, which is stabilized by the two-dimensional (2D) wallpaper group $P2gg$, we anticipate to observe two intertwined drumhead surface states (DSSs) [12]. At the $\bar{S}$ point, $\mathcal{T} = \mathcal{K}$, and $\mathcal{T}$ should commute with all spatial symmetries. Since both $\mathcal{G}_x$ and $\mathcal{G}_y$ should take the eigenvalues $\pm i$, the symmetry constraints can be determined as $\mathcal{G}_x = i\mu_2$, $\mathcal{G}_y = i\mu_2$, where $\mu_{1,2,3}$ are Pauli matrices acting in orbital space. The DSS, shown schematically in Fig. 2(d), can be described by the $k \cdot p$ Hamiltonian around the $\bar{S}$ point,

$$H_{DSS}(q_x, q_y) = q_x q_y (a_3\mu_3 + a_1\mu_1), \quad (7)$$

where $a_{1,3}$ are real constants. Two saddle-like hyperbolic paraboloids (red and gray surfaces in Fig. 2(d)) are intertwined with each other, resulting in the doubly degenerate bands along $\bar{S}-\bar{X}$ and $\bar{S}-\bar{Y}$ respectively, which are enforced by $\mathcal{G}_x$ and $\mathcal{G}_y$ symmetries combined with $\mathcal{T}$. We would like to emphasize that these remarkable features exhibited by the new DSSs allow them to provide a great platform for studies of exotic emergent phenomena.

The calculated (001) surface band structure along $\bar{X} - \bar{S} - \bar{\Gamma}$ for $|\lambda_{10}| < |\lambda_{13}|$ is shown in Fig. 2(e). Intriguingly, we notice that another type of DSSs, shown in Fig. 2(f), can be realized when $|\lambda_{10}| > |\lambda_{13}|$ with all remaining parameters unchanged. We refer to the two different types of DSSs as type-I/type-II for the former/latter case. Type-II DSSs can be comprehended from the way one proceeds to decompose the second pair of CICE into two single NLs. As shown in Fig. 1(b) the NLs (shown by magenta color) are allowed by the same band configurations with swapped conduction bands in comparison to the configurations of Fig. 1 (a). In contrast to the NLs of the half-filling CICE, the NLs labeled in magenta are due to the crossings between two occupied bands (one-quarter filling) and two unoccupied bands (three-quarter filling), respectively, and hence might be irrelevant for electron excitation at half-filling system. However, the CICE TSM introduces another possibility. As one cannot distinguish whether the FDPs of CICE belong to the half-filling CICE or the second pair of CICE, both of them can provide topological DSSs on an equal footing due to the inherent band inversion. Even though both types of NL contribute to the DSS on the (001) surface, $\mathcal{G}_x$ and $\mathcal{G}_y$ permit solely one pair of DSSs, forcing in turn the other pair merge into the bulk states. Consequently, the DSS of CICE-NL in the *spinless* case may appear in either way depending on the coupling parameter details.

MATERIAL CANDIDATES

We propose a series of compounds as material candidates for the experimental realization of this new type of TSMs that host butterfly-like CICE NLs, such as ZrX_2 (X = As, P) with CICE centered at TRIM point U $(\pi, \pi, 0)$, as well as Tl_2GeTe_5, CYB_2 and Al_2Y_3 at M $(\pi, \pi, 0)$, respectively. Here we take the $ZrAs_2$ and Tl_2GeTe_5 as representatives. The equilibrium lattice constants and electronic structure of both compounds were determined by first principles density functional theory (DFT) calculations using the VASP [30] and WIEN2k [31] packages CYB_2 and Al_2Y_3 were found using the *Advanced Search Tools* of https://www.topologicalquantumchemistry.org/[32–35], see Appendix C for details).

The crystal structure of $ZrAs_2$, is orthorhombic with SG *Pnma* (No. 62) and is displayed in Fig. 3 (a). The calculated lattice parameters $a = 6.847$ Å, $b = 3.718$ Å and $c = 9.123$ Å are in agreement with the experimental ones [36, 37]. The band structure without spin-orbit coupling (SOC) close to the $U = (\pi, 0, \pi)$ point of the BZ is shown in Fig. 3 (b) along two high-symmetry lines

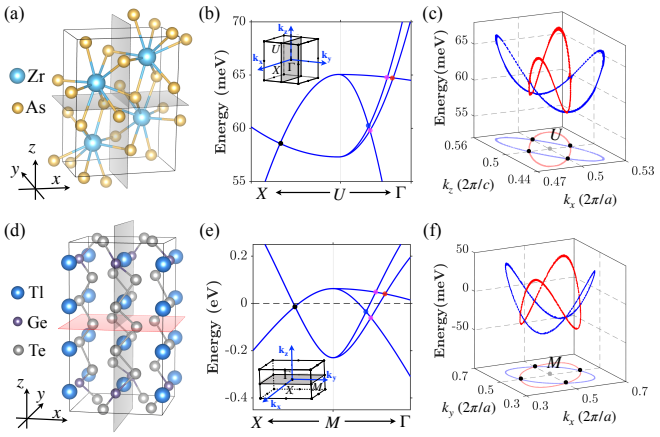

FIG. 3. Crystal structure of bulk (a) $ZrAs_2$ and (d) Tl_2GeTe_5. Band structure of (b) $ZrAs_2$ and (e) Tl_2GeTe_5 close to the Fermi energy without spin-orbit coupling (SOC) along the symmetry lines in the BZ shown in the insets where high-symmetry points are marked. The relevant crossings on U (M)-Γ for the half-filling and the second pair of CICE are indicated by [red, blue] and magenta dots, respectively. Energy-momentum spread for the half-filing CICE nodal lines in the BZ for (c) $ZrAs_2$ centered at U point on the (010) plane (grey shaded) and (f) Tl_2GeTe_5 at M point on the (001) plane (grey shaded). The black dots shown on the projected CICEs in the k space are the FDPs and one of them is indicated in the band along X-U (M) of (b) and (e). As suggested by the crossings in (b) and (e), the energy spreads for the second pair of CICE are very similar.

($X-U$ and $U-\Gamma$). The second material, Tl_2GeTe_5, has tetragonal structure with SG $P4/mbm$ (No. 127) and the crystal structure is depicted in Fig. 3 (d). In the DFT calculations the experimental structure of Tl_2GeTe_5 [38, 39] is applied, and the band structures along two essential high symmetry k paths $M \to X$ and $M \to \Gamma$ are shown in Fig. 3 (d), which reveal band crossings alike those observed in $ZrAs_2$.

In order to corroborate the CICE NLs in $ZrAs_2$ around U we used the Bloch functions obtained with DFT to construct a Wannier-function based model employing the Wannier90 package[40]. The model reproduces the bands around the Fermi level, allowing the scan of band crossings in the BZ more efficiently than direct DFT calculations. As shown in Fig. 3 (c) the nodal points around U point form a butterfly-like CICE with a small energy dispersion. In the case of Tl_2GeTe_5, the band crossings, shown in Fig 3 (f), occur closer to the M point, yielding a smaller area enclosed by the CICE and a lower energy dispersion.

CONCLUSION

In summary, we have proposed a new type of TSMs which unveil intriguing butterfly-like CICE NLs. We have derived the symmetry criteria to generate the CICE, identified the 9 SGs which can host such complex NLs and determined the positions of the CICE centers in the BZ for each SG. In one of the SGs *Pbam* (No. 55), we have introduced a model of *spinless* fermions, which hosts CICE and supports the intriguing two intertwined DSSs. We have also calculated the Zak phase, which is related to the bulk-boundary correspondence [41–48] (see details in Appendix B). In our following work [49], we have investigated the effect of SOC on a CICE TSM, where the connection of the CICE NLSM and the TCI protected by glide symmetries is revealed. More specifically, the intertwined DSSs evolve to topological surface states (TSSs) with four-fold Dirac fermion. In addition, a 3D HOTI protected by glide symmetry emerges in the presence of SOC. The appearance of a pair of doubly degenerate saddle-points or Van Hove Singularities on the surface states, provides a platform for exploring the interplay between topological states and the physics of strongly correlated systems, e.g., the related interaction-driven instabilities, such as superconducting states and charge-density-wave (CDW) phase.

Finally, we have predicted candidate materials which can host such exotic NL landscapes. Many materials may have substantial SOC, which would lift the band crossings and drive the system to an insulating phase. However, for materials with negligible SOC, the band gaps lifted by SOC might be small. Hence, those observable physical properties, *e.g.* electronic transport, still hold. In addition, this model also can be realized in other *spinless* fermion systems, such as photonic crystals. In general, the study of the material band structures without SOC provides some clues and indicate the connections between a topological semimetal phase (without SOC) and a topological insulating phase (with SOC) [49]. We hope that these predictions will motivate experimental studies of such complex NLs. For instance, the optical and magneto-optical signatures of CICE nodal lines are worth investigating.

ACKNOWLEDGMENTS

The work at CSUN was supported by NSF-Partnership in Research and Education in Materials (PREM) Grant No. DMR-1828019. The work of J.L.M. has been supported by Spanish Science Ministry grant PGC2018-094626-B-C21 (MCIU/AEI/FEDER, EU) and Basque Government grant IT979-16. M.G.V. and M.I. acknowledge support from the Span-ish Ministerio de Ciencia e Innovacion (grants numberPID2019-109905GB-C21 and PGC2018-094626-B-C21) and Basque Government (grant IT979-16). H.L. acknowledges the support by the Ministry of Science and Technology (MOST) in Taiwan under grant number MOST 109-2112-M-001-014-MY3.

APPENDIX A: SYMMETRY CONSTRAINTS

According to the analysis in main text, a model which hosts the CICE nodal lines requires at least four bands. Now we try to construct a Hamiltonian in space group (SG) *Pbam* (No. 55), in which there are four sets of Wyckoff positions, *i.e.* 2a, 2b, 2c and 2d. Each of them contains two sublattices (denoted by A and B). Thus, to construct a 4-band minimal model, two orbitals from each sublattice are required.

The coordinates of the two sublattices for each set of Wyckoff positions are listed here. 2*a*: $(0,0,0)$, $(\frac{1}{2},\frac{1}{2},0)$; 2*b*: $(0,0,\frac{1}{2})$, $(\frac{1}{2},\frac{1}{2},\frac{1}{2})$; 2*c*: $(\frac{1}{2},0,0)$, $(0,\frac{1}{2},0)$; 2*d*: $(\frac{1}{2},0,\frac{1}{2})$, $(0,\frac{1}{2},\frac{1}{2})$. One can find that for any set of Wyckoff positions, sublattice A(B) maps to A(B) under the mirror symmetry $\mathcal{M}_z$, or inversion symmetry $\mathcal{I}$. That indicates that the constraints of both $\mathcal{M}_z$ and $\mathcal{I}$ should be written as τ_0 (identity matrix) employing the basis $(A,B)^T$, and the eigenvalue can only be the single value 1. Therefore, the two orbitals selected should carry opposite parity and eigenvalues of $\mathcal{M}_z$, so that the nodal line band crossings in (001) plane are protected due to the opposite eigenvalues of mirror symmetry. Indeed, the choices of the Wyckoff positions or orbitals are not unique, *e.g.* $(s,\, p_z)$, $(p_x,\, d_{yz})$ and $(p_y,\, d_{xz})$.

Here we choose two sublattices denoted by A and B occupying the 2*a* Wyckoff position at $\mathbf{r}_A = (0,0,0)$ and $\mathbf{r}_B = (\frac{1}{2},\frac{1}{2},0)$ in a unit cell, and each sublattice has two electrons of orbitals p_z and d_{xy}. Employing the basis $\Psi = (p_z^A, d_{xy}^A, p_z^B, d_{xy}^B)^T$, the symmetry constraints at TRIM points take the form

$$
\begin{aligned}
&\Gamma=(0,0,0)\cup Z=(0,0,\pi): \quad \mathcal{T}=\mathcal{K},\ \ \mathcal{I}=-\sigma_3,\quad \mathcal{M}_z=-\sigma_3,\ \ \mathcal{G}_x=e^{-iq_y/2}\tau_1\sigma_3,\ \ \mathcal{G}_y=e^{-iq_x/2}\tau_1\sigma_3.\\
&S=(\pi,\pi,0)\cup R=(\pi,\pi,\pi): \quad \mathcal{T}=\mathcal{K},\ \ \mathcal{I}=-\sigma_3,\quad \mathcal{M}_z=-\sigma_3,\ \ \mathcal{G}_x=-e^{-iq_y/2}i\tau_2\sigma_3,\ \ \mathcal{G}_y=-e^{-iq_x/2}i\tau_2\sigma_3.\\
&X=(\pi,0,0)\cup U=(\pi,0,\pi): \quad \mathcal{T}=\tau_3\mathcal{K},\ \ \mathcal{I}=-\tau_3\sigma_3,\quad \mathcal{M}_z=-\sigma_3,\ \ \mathcal{G}_x=e^{-iq_y/2}\tau_2\sigma_3,\ \ \mathcal{G}_y=-e^{-iq_x/2}i\tau_1\sigma_3.\\
&Y=(0,\pi,0)\cup T=(0,\pi,\pi): \quad \mathcal{T}=\tau_3\mathcal{K},\ \ \mathcal{I}=-\tau_3\sigma_3,\quad \mathcal{M}_z=-\sigma_3,\ \ \mathcal{G}_x=-e^{-iq_y/2}i\tau_1\sigma_3,\ \ \mathcal{G}_y=e^{-iq_x/2}\tau_2\sigma_3.
\end{aligned}
\tag{A1}
$$

where $q_{x,y}$ is the k vector from the corresponding TRIM point, Pauli matrices τ and σ are used for the sublattice and orbital space respectively, and $\mathcal{K}$ is the complex conjugate operator. Given these constrains, the minimal tight-binding model can be constructed.

APPENDIX B: THE ZAK PHASE

The Zak phase γ has been used for the $\mathbb{Z}_2$ classification of inversion-symmetric one-dimensional (1D) insulators, where it can be quantized to 0 or π (mod 2π). It can be also applied to the effective 1D models along one direction by fixing one or two momenta of two-dimensional (2D) or three-dimensional (3D) Hamiltonians. In this $\mathbb{Z}_2$ classification, the bulk-boundary correspondence states that, the nontrivial Zak phase $\gamma=\pi$ indicates the emergence of boundary modes, while $\gamma=0$ is considered a trivial insulator without surface modes. In our model, the CICE NLs consisting of two ellipses lie on $k_z=0$ plane. Considering k_x and k_y as parameters, we calculate the Zak phase of the 1D model along the k_z direction, and the CICE NLs are projected on the (k_x,k_y)-plane (FIG. A1(a)). Within the areas of the projection of each one single nodal line, the Zak phase is π, indicating the emergence of one DSS (area labeled in yellow in FIG. A1(b)). However, within the overlapping area of the projections of two NLs, the Zak phase is 0 (FIG. A1(b)), although there are two copies of DSSs. This implies that, the even number of DSSs cannot be characterized by the Zak phase, and is invisible in the $\mathbb{Z}_2$ classification.

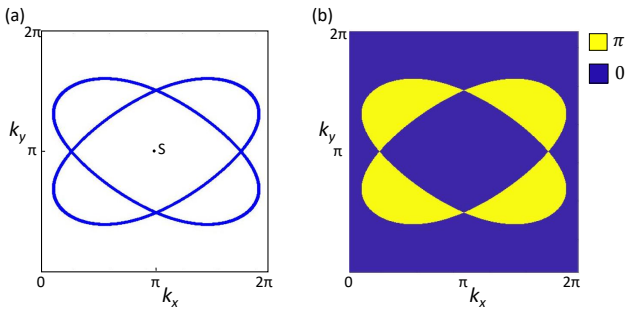

FIG. A1. (a) CICE nodal lines around S point on $k_z=0$ plane. (b) The Zak phase γ distributions for the model. The yellow (blue) color represents π (0). Outside the projection of the NLs, no surface modes can be observed and the Zak phase $\gamma=0$, while within the area labeled in yellow, there is one DSS. However, within the overlapping area of the projections of two NLs, the Zak phase is 0 (mod 2π), although there are two DSSs within that area, which cannot be characterized by the $\mathbb{Z}_2$ Zak phase.

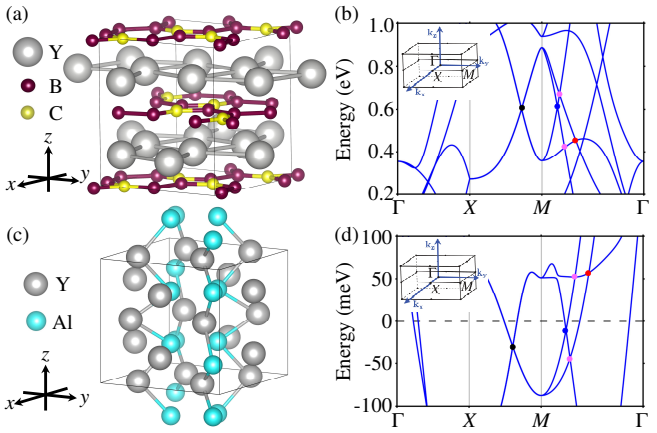

FIG. A2. Crystal structure of bulk (a) CYB_2 with tetragonal space group (SG) $P4_2/mbc$ (No.135), (c) Al_2Y_3 with tetragonal SG $P4/mbm$ (No. 136). Band structure of (b) CYB_2 and (d) Al_2Y_3 close to the Fermi energy without spin-orbital coupling (SOC) along the symmetry lines in the Brillouin zone shown in the insets where high-symmetry points are marked. The relevant crossings on M-Γ for the half-filling and the second pair of CICE are indicated by [red, blue] and magenta dots, respectively. The black dots along X-M are the fourfold degenerate points (FDPs).

APPENDIX C: OTHER MATERIAL CANDIDATES

We propose CYB_2[50] and Al_2Y_3[51] as materials candidates to host CICE. The crystal structure of CYB_2 is tetragonal with SG $P4_2$/mbc (No.135) and shows a layered structured of Y layers intercalated with B and C nets. Al_2Y_3 crystal structured belongs to $P4_2$/mnm (No. 136) tetragonal SG. Figs. A2 (a) - (c) and (b) - (d) show the band structure calculation and crystal structure of CYB_2 and Al_2Y_3 respectively. The band structures include two essential high symmetry paths $X \to \Gamma \to M$, where the crossings of CICE are highlighted by black dots. These bands structures were calculated using VASP with the the modified Becke-Johnson exchange potential in combination with GGA [52, 53]. The BZ was sampled with a $7 \times 7 \times 9$ Monkhorst-Pack grid and an energy cut off of 520 eV was used.

APPENDIX D: DETAILS OF THE CALCULATIONS

In the density functional theory (DFT) calculations of $ZrAs_2$ and ZrP_2 the Perdew-Burke-Ernzherhof (PBE) [54] implementation of the generalized gradient approximation (GGA) was used for the exchange-correlation functional. A plane-wave basis with an energy cutoff of 340 eV was employed in all calculations. The BZ was sampled with an 8×15×6 Monkhorst-Pack grid [55]. The systems were allowed to fully relax until residual atomic forces became smaller than 0.01 eV/Å.

Turning on the SOC in $ZrAs_2$ opens a small gap of about 8 meV of the band crossings around the U point. Furthermore, we have carried out electronic structure calculations using the MBJ exchange correlation functional which predicts band gaps, effective masses, and frontier-band ordering that are in good agreement with the computationally more intense GW and hybrid functional approaches [56]. The calculations reveal that the band crossings around the U point in $ZrAs_2$ disappear indicating that the CICEs (and the closing of the gap) is very sensitive to the exchange-correlation functional employed.

A Wannier function-based model for $ZrAs_2$ and ZrP_2 was obtained using the DFT results as starting point. The Wannier90 package along with its interface with the VASP package were employed for this purpose [40] The upper limit of the frozen energy window was set to 2.5 eV above the Fermi level of each compound. The model perfectly reproduces the DFT bands up to that energy, which is well above the studied band crossings. We chose the following atomic orbitals as the starting guess for the projection of the Bloch states onto Wannier functions: s, p and d orbitals for Zr and s and p orbitals for As or P.

* physxtzhou@gmail.com
† nick.kioussis@csun.edu

[1] C. Fang, Y. Chen, H.-Y. Kee, and L. Fu, Phys. Rev. B **92**, 081201(R) (2015).
[2] C. Fang, H. Weng, X. Dai, and Z. Fang, Chinese Physics B **25** (2016), 10.1088/1674-1056/25/11/117106.
[3] H. Weng, X. Dai, and Z. Fang, Journal of Physics Condensed Matter **28** (2016), 10.1088/0953-8984/28/30/303001.
[4] N. P. Armitage, E. J. Mele, and A. Vishwanath, Reviews of Modern Physics **90**, 015001 (2018).
[5] X. Wan, A. M. Turner, A. Vishwanath, and S. Y. Savrasov, Physical Review B **83**, 205101 (2011).
[6] A. A. Burkov and L. Balents, Physical Review Letters **107**, 127205 (2011).
[7] S. M. Young, S. Zaheer, J. C. Y. Teo, C. L. Kane, E. J. Mele, and a. M. Rappe, Physical Review Letters **108**, 140405 (2012).
[8] Z. Wang, Y. Sun, X. Q. Chen, C. Franchini, G. Xu, H. Weng, X. Dai, and Z. Fang, Physical Review B **85**, 195320 (2012).
[9] S. M. Young and C. L. Kane, Physical Review Letters **115**, 126803 (2015).
[10] T.-R. Chang, S.-Y. Xu, D. S. Sanchez, W.-F. Tsai, S.-M. Huang, G. Chang, C.-H. Hsu, G. Bian, I. Belopolski, Z.-M. Yu, S. A. Yang, T. Neupert, H.-T. Jeng, H. Lin, and M. Z. Hasan, Physical Review Letters **119**, 026404 (2017).
[11] W. C. Yu, X. Zhou, F.-C. Chuang, S. A. Yang, H. Lin, and A. Bansil, Physical Review Materials **2**, 051201 (2018).
[12] A. A. Burkov, M. D. Hook, and L. Balents, Physical

Review B **84**, 235126 (2011).
[13] S.-Y. Xu, I. Belopolski, N. Alidoust, M. Neupane, G. Bian, C. Zhang, R. Sankar, G. Chang, Z. Yuan, C.-C. Lee, S.-M. Huang, H. Zheng, J. Ma, D. S. Sanchez, B. Wang, A. Bansil, F. Chou, P. P. Shibayev, H. Lin, S. Jia, and M. Z. Hasan, Science **349**, 613 (2015).
[14] G. Bian, T.-R. Chang, H. Zheng, S. Velury, S.-Y. Xu, T. Neupert, C.-K. Chiu, S.-M. Huang, D. S. Sanchez, I. Belopolski, N. Alidoust, P.-J. Chen, G. Chang, A. Bansil, H.-T. Jeng, H. Lin, and M. Z. Hasan, Physical Review B **93**, 121113 (2016).
[15] A. A. Burkov, Physical Review Letters **113**, 247203 (2014).
[16] C.-L. Zhang, S.-Y. Xu, I. Belopolski, Z. Yuan, Z. Lin, B. Tong, G. Bian, N. Alidoust, C.-C. Lee, S.-M. Huang, T.-R. Chang, G. Chang, C.-H. Hsu, H.-T. Jeng, M. Neupane, D. S. Sanchez, H. Zheng, J. Wang, H. Lin, C. Zhang, H.-Z. Lu, S.-Q. Shen, T. Neupert, M. Zahid Hasan, and S. Jia, Nature Communications **7**, 10735 (2016).
[17] J. Hu, S.-Y. Xu, N. Ni, and Z. Mao, Annual Review of Materials Research **49**, 207 (2019).
[18] T. Bzdušek, Q. S. Wu, A. Rüegg, M. Sigrist, and A. A. Soluyanov, Nature **538**, 75 (2016).
[19] G. Chang, S. Y. Xu, X. Zhou, S. M. Huang, B. Singh, B. Wang, I. Belopolski, J. Yin, S. Zhang, A. Bansil, H. Lin, and M. Z. Hasan, Physical Review Letters **119**, 1 (2017).
[20] Z. Yan, R. Bi, H. Shen, L. Lu, S. C. Zhang, and Z. Wang, Physical Review B **96**, 1 (2017).
[21] R. Bi, Z. Yan, L. Lu, and Z. Wang, Physical Review B **96**, 201305 (2017).
[22] B.-J. Yang and N. Nagaosa, Nature Communications **5**, 4898 (2014).
[23] Z. Gao, M. Hua, H. Zhang, and X. Zhang, Physical Review B **93**, 205109 (2016).
[24] B. J. Wieder, Y. Kim, A. M. Rappe, and C. L. Kane, Physical Review Letters **116**, 186402 (2016).
[25] Z. Zhu, G. W. Winkler, Q. Wu, J. Li, and A. A. Soluyanov, Physical Review X **6**, 031003 (2016).
[26] C. Gong, Y. Xie, Y. Chen, H.-S. Kim, and D. Vanderbilt, Physical Review Letters **120**, 106403 (2018).
[27] S. Ahn, E. J. Mele, and H. Min, Phys. Rev. Lett. **119**, 147402 (2017).
[28] Y. Shao, Z. Sun, Y. Wang, C. Xu, R. Sankar, A. J. Breindel, C. Cao, M. M. Fogler, A. J. Millis, F. Chou, Z. Li, T. Timusk, M. B. Maple, and D. N. Basov, Proceedings of the National Academy of Sciences **116**, 1168 (2019), https://www.pnas.org/content/116/4/1168.full.pdf.
[29] Z. Wang, A. Alexandradinata, R. J. Cava, and B. A. Bernevig, Nature **532**, 189 (2016).
[30] G. Kresse and J. Hafner, Physical Review B **48**, 13115 (1993).
[31] P. Blaha, K. Schwarz, F. Tran, R. Laskowski, G. K. H. Madsen, and L. D. Marks, The Journal of Chemical Physics **152**, 074101 (2020).
[32] B. Bradlyn, L. Elcoro, J. Cano, M. G. Vergniory, Z. Wang, C. Felser, M. I. Aroyo, and B. A. Bernevig, Nature **547**, 298 EP (2017), article.
[33] M. G. Vergniory, L. Elcoro, C. Felser, N. Regnault, B. A. Bernevig, and Z. Wang, Nature **566**, 480 (2019).
[34] T. Zhang, Y. Jiang, Z. Song, H. Huang, Y. He, Z. Fang, H. Weng, and C. Fang, Nature **566**, 475 (2019).
[35] F. Tang, H. C. Po, A. Vishwanath, and X. Wan, Nature **566**, 486 (2019).
[36] W. Trzebiatowski, S. Weglowski, and L. Lukaszewicz, Roczn. Chem. **32**, 189 (1958).
[37] P. E. Blanchard, R. G. Cavell, and A. Mar, Journal of alloys and compounds **505**, 17 (2010).
[38] R. Marsh, Journal of Solid State Chemistry **87**, 467 (1990).
[39] A. Abba Toure, G. Kra, R. Eholie, J. Olivier Fourcade, J. Jumas, and M. Maurin, Journal of Solid State Chemistry **84**, 245 (1990).
[40] A. A. Mostofi, J. R. Yates, Y.-S. Lee, I. Souza, D. Vanderbilt, and N. Marzari, Computer Physics Communications **178**, 685 (2008).
[41] J. Zak, Phys. Rev. Lett. **62**, 2747 (1989).
[42] R. D. King-Smith and D. Vanderbilt, Phys. Rev. B **47**, 1651 (1993).
[43] D. Vanderbilt and R. D. King-Smith, Phys. Rev. B **48**, 4442 (1993).
[44] S. Ryu and Y. Hatsugai, Phys. Rev. B **73**, 245115 (2006).
[45] T. Kariyado and Y. Hatsugai, Phys. Rev. B **88**, 245126 (2013).
[46] F. Grusdt, M. Höning, and M. Fleischhauer, Phys. Rev. Lett. **110**, 260405 (2013).
[47] R. Barnett, Phys. Rev. A **88**, 063631 (2013).
[48] Y.-H. Chan, C.-K. Chiu, M. Y. Chou, and A. P. Schnyder, Phys. Rev. B **93**, 205132 (2016).
[49] X. Zhou, C.-H. Hsu, C.-Y. Huang, M. Iraola, J. L. Mañes, M. G. Vergniory, H. Lin, and N. Kioussis, arXiv:2005.06071 (2020).
[50] J. Bauer and J. Debuigne, Journal of Inorganic and Nuclear Chemistry **37**, 2473 (1975).
[51] T. Dagerhamn, Arkiv foer Kemi **27**, 363 (1967).
[52] A. D. Becke and E. R. Johnson, The Journal of Chemical Physics **124**, 221101 (2006), https://doi.org/10.1063/1.2213970.
[53] F. Tran and P. Blaha, Phys. Rev. Lett. **102**, 226401 (2009).
[54] J. P. Perdew, K. Burke, and M. Ernzerhof, Physical Review Letters **77**, 3865 (1996).
[55] H. J. Monkhorst and J. D. Pack, Physical Review B **13**, 5188 (1976).
[56] Y.-S. Kim, M. Marsman, G. Kresse, F. Tran, and P. Blaha, Phys. Rev. B **82**, 205212 (2010).